

Inclination instability of circumbinary planets

Stephen H. Lubow^{1*}, Anna C. Childs² and Rebecca G. Martin^{3,4}

¹*Space Telescope Science Institute, 3700 San Martin Drive, Baltimore, MD 21218, USA*

²*Center for Interdisciplinary Exploration and Research in Astrophysics (CIERA) and Department of Physics and Astronomy Northwestern University, 1800 Sherman Ave, Evanston, IL 60201 USA*

³*Nevada Center for Astrophysics, University of Nevada, Las Vegas, 4505 S. Maryland Pkwy., Las Vegas, NV 89154, USA*

⁴*Department of Physics and Astronomy, University of Nevada, Las Vegas, 4505 S. Maryland Pkwy., Las Vegas, NV 89154, USA*

Accepted April 9, 2024. Received March 19, 2024; in original form January 24, 2024

ABSTRACT

We analyze a tilt instability of the orbit of an outer planet in a two planet circumbinary system that we recently reported. The binary is on an eccentric orbit and the inner circumbinary planet is on a circular polar orbit that causes the the binary to undergo apsidal precession. The outer circumbinary planet is initially on a circular or eccentric orbit that is coplanar with respect to the binary. We apply a Hamiltonian in quadrupole order of the binary potential to show that the tilt instability is the result of a secular resonance in which the apsidal precession rate of the binary matches the nodal precession rate of the outer planet. Resonance is possible because the polar inner planet causes the apsidal precession of the binary to be retrograde. The outer planet periodically undergoes large tilt oscillations for which we analytically determine the initial evolution and maximum inclination. Following a typically relatively short adjustment phase, the tilt grows exponentially in time at a characteristic rate that is of order the absolute value of the binary apsidal precession rate. The analytic results agree well with numerical simulations. This instability is analogous to the Kozai-Lidov instability, but applied to a circumbinary object. The instability fails to operate if the binary mass ratio is too extreme. The instability occurs even if the outer planet is instead an object of stellar mass and involves tilt oscillations of the inner binary.

Key words: celestial mechanics, planetary systems, methods: analytic, methods: numerical, binaries: general

1 INTRODUCTION

About a dozen circumbinary planets have been detected through transits with the Kepler and TESS telescopes. All of these planets are nearly coplanar with the orbit of the binary. This is largely a selection effect due to the technique adopted (Schneider 1994; Martin & Triaud 2014, 2015; Martin 2017; Zhang & Fabrycky 2019). Estimates suggest that the frequency of these observed circumbinary planets is similar to that around single stars, once the selection effects are taken into account (Li et al. 2016). On this basis one might conclude that there is not a large population of noncoplanar circumbinary planets.

However, misaligned planets are more likely to be found around longer period binaries than the planets found in current observations. Circumbinary planets are expected to form in circumbinary discs. Circumbinary discs are often found in observations to be misaligned (Czekala et al. 2019). If the binary orbit is sufficiently eccentric, the protostellar disc could increase its inclination and evolve to a polar state in which it is perpendicular to the binary orbital plane (Aly et al. 2015; Martin & Lubow 2017; Lubow & Martin 2018; Zanazzi & Lai 2018; Cuello & Giuppone 2019; Smallwood et al. 2020). Due to tidal dissipation, closer binaries, with periods less than about 10 days, tend to have low eccentricity (Goldman & Mazeh 1991; Raghavan et al. 2010), which is unfavorable for the growth of disc inclination.

Circumbinary discs around low eccentricity binaries typically evolve to coplanarity (Nixon et al. 2011; Facchini et al. 2013; Foucart & Lai 2014). Most of the detected circumbinary planets are found around such lower eccentricity binaries. At longer binary orbital periods, circumbinary discs are more likely to be misaligned with respect to the binary, since the binary eccentricities are typically larger. Observations suggest that circumbinary discs in orbit around binaries with periods longer than about 30 days tend to be misaligned with respect to the binary (Czekala et al. 2019). In addition, two polar gas discs and one polar debris disc have been detected and both involve highly eccentric binaries ($e \sim 0.8$) (Kennedy et al. 2012, 2019; Kenworthy et al. 2022).

Since there may be a population of misaligned circumbinary planets, some recent studies have examined their predicted properties (e.g., Verrier & Evans 2009; Farago & Laskar 2010; Doolin & Blundell 2011; Naoz et al. 2017; Quarles et al. 2018; Chen et al. 2019). The orbit of a slightly misaligned planet around an eccentric orbit binary undergoes circulation in which its line of nodes pass through all 360° and the angular momentum vector precesses around the binary angular momentum vector. Because the binary is eccentric, the orbit of the planet undergoes tilt oscillations. But at higher levels of initial misalignment, the orbit of the planet can undergo libration in which its line of nodes passes through a limited angular range, less than 360° . In this case, the planet’s angular momentum vector precesses around the binary eccentricity vector, rather than around

* E-mail: lubow@stsci.edu

the binary angular momentum vector. [Chen et al. \(2019\)](#) analyzed the properties of these orbits as a function of planet mass. [Chen et al. \(2020\)](#) studied the stability of noncoplanar circumbinary planets and found that the polar configuration is the most stable at high binary eccentricity.

More recently, some studies have concentrated on the form of planet orbits and their stability when there are two interacting planets (e.g. [Chen et al. 2023a](#)). [Chen et al. \(2022\)](#) considered a configuration in which both planet orbits are initially mutually coplanar, but misaligned relative to the orbit plane of the binary. Planet-planet interactions can lead to complex tilt oscillations of each planet because two torques operate at independent frequencies: the nodal precession frequency due to the binary and the nodal precession frequency due to the relative nodal precession of the two planets. In addition, circumbinary planet-planet interactions can make the planet orbit much less stable than would occur for a single circumbinary planet or two interacting planets around a single star ([Chen et al. 2023b](#)).

Recently [Childs et al. \(2023\)](#) investigated the orbital evolution of a two planet circumbinary system in which the planets are mutually initially highly misaligned. The inner planet is on a polar orbit, while the outer planet is coplanar with the orbit of the binary. Such a configuration could develop from planet formation in a broken disk ([Nixon et al. 2013](#); [Facchini et al. 2013](#); [Lubow & Martin 2018](#); [Martin & Lubow 2018, 2019](#)) or, from multiple epochs of disc formation ([Bate 2018](#)). The inner planet is assumed to be sufficiently far from the outer planet that the direct planet-planet interactions are small compared to the effects of the binary on the outer planet. The surprising result is that the outer planet undergoes large tilt oscillations away from the coplanar configuration. Some analytic estimates were made for the radial range over which this effect operates. The purpose of this paper is to further explore the dynamics of this configuration.

In Section 2 we describe an analytic model for the orbital evolution of the outer planet. In Section 3 we describe a geometric explanation for qualitative features of the analytic model. Section 4 describes some results of simulations and makes a comparison with the predictions of the analytic model. It discusses how the instability operates if the binary mass ratio is extreme or if the outer object is massive. Sections 5 and 6 contain the discussion and summary, respectively.

2 ANALYTIC MODEL

We consider a binary star system of mass m_b with component masses m_1 and m_2 that is on an orbit with semi-major axis a_b , eccentricity e_b , and orbital frequency Ω_b . The binary undergoes apsidal precession at a rate $d\varpi_b/dt$, where ϖ_b is the longitude of periastris of the binary. We consider two circumbinary planets. The inner planet with mass m_3 is on a circular polar orbit with semi-major a_3 . The outer planet is modeled as a test particle, $m_4 = 0$. The outer planet has orbital elements that are denoted with the notation a_4, e_4, i, ω_4 , and Ω_4 for its semi-major axis, eccentricity, inclination with respect to the binary orbital plane, argument of periastris, and longitude of ascending node in the inertial frame, respectively. The orbit may have an initial eccentricity and is initially nearly coplanar with respect to the binary.

As shown in [Childs et al. \(2023\)](#), the gravitational forcing of the outer planet by the inner planet can typically be ignored compared with the forcing by the binary, provided that the two planets are well separated. The inner planet causes the binary to undergo apsidal precession. The Hamiltonian that describes the motion of the outer planet then depends on the binary parameters and its precession rate. We apply a Hamiltonian to quadrupole order in the binary potential. We note that in the case that the outer planet is on a circular orbit

or the binary has equal mass members, the octupole order terms vanish (e.g., equation (7) of [de Elía et al. 2019](#)) and the quadrupole approximation is expected to be more accurate.

2.1 Hamiltonian

A secular Hamiltonian is obtained by averaging the potential due to the binary over a binary orbit period and averaging that potential on the outer planet over its orbital period. The secular equations of motion for the orbital elements of the outer planet are derived from the secular Hamiltonian. In the absence of the inner planet, the binary orbit is fixed in the inertial frame. The unperturbed Hamiltonian is obtained by considering the binary to be a single point mass. The equations of motion for the outer planet are derived from the perturbed Hamiltonian that is due to tidal effects of the binary. The secular perturbed Hamiltonian per unit mass of the outer planet for the nonprecessing binary (np) to quadrupole order in the binary potential is given by

$$H_{\text{np}} = \frac{\alpha}{(1 - e_b^2)^{3/2}} \left[(2 + 3e_b^2)(1 - 3\cos^2(i_4)) - 15e_b^2 \cos(2\Omega_4) \sin^2 i_4 \right], \quad (1)$$

where

$$\alpha = \frac{1}{16} \frac{m_1 m_2}{m_b^2} \frac{a_b^5}{a_4^3} \Omega_b^2 \quad (2)$$

(e.g., [Farago & Laskar 2010](#); [Naoz et al. 2017](#)) and the binary angular frequency is $\Omega_b = \sqrt{Gm_b/a_b^3}$. This Hamiltonian is expressed in terms of orbital elements. Appendix A describes the Hamiltonian with Delaunay canonical variables.

In the presence of the inner planet, the binary undergoes apsidal precession at rate $d\varpi_b/dt$. The orbit of the outer planet is best described in the frame that precesses with the binary (e.g., [Farago & Laskar 2010](#); [Zanardi et al. 2018, 2023](#)). In that frame, the inclination is a single valued function of nodal phase (modulo 360°) over all times. Consequently, we analyze the motion of the outer planet in the frame that precesses with the binary. In transforming to this frame, we replace Ω_4 by the value of the longitude of the ascending node in the rotating frame, denoted as ϕ_4 , while inclination i_4 remains unchanged from its value in the nonrotating frame. The transformation is described in more detail using Delaunay canonical variables in Appendix A. The Hamiltonian H_{np} is transformed to a Hamiltonian that accounts for the frame rotation by adding a term (see Appendix D of [Tremaine 2023](#)). The added term is $-\Omega_f \cdot L_4$, where Ω_f is the rotation rate of the frame and L_4 is the angular momentum per unit mass of the outer planet with magnitude

$$L_4 = a_b^{3/2} \Omega_b \sqrt{a_4(1 - e_4^2)}. \quad (3)$$

In a frame that rotates with the binary eccentricity vector, the Hamiltonian becomes

$$H = \frac{\alpha}{(1 - e_b^2)^{3/2}} \left[(2 + 3e_b^2)(1 - 3\cos^2(i_4)) - 15e_b^2 \cos(2\phi_4) \sin^2 i_4 \right] - L_4 \frac{d\varpi_b}{dt} \cos(i_4). \quad (4)$$

In this equation ϕ_4 is the longitude of the ascending node of the outer planet in the corotating frame, i.e., relative to the instantaneous

eccentricity vector of the binary. The apsidal precession rate of the binary due to the polar planet is given by

$$\frac{d\varpi_b}{dt} = -\frac{9}{4} \frac{m_3}{m_b} \left(\frac{a_b}{a_3}\right)^3 \sqrt{1-e_b^2} \Omega_b \quad (5)$$

(e.g., Innanen et al. 1997; Naoz 2016; Zhang & Fabrycky 2019; Childs et al. 2023).

2.2 Equations of Motion

We apply Hamilton's equations with Delanuy variables to the Hamiltonian given by Equation (4) (see Appendix A) to obtain

$$\frac{da_4}{dt} = 0, \quad (6)$$

$$\frac{de_4}{dt} = 0, \quad (7)$$

$$\frac{di_4}{dt} = \frac{1}{L_4 \sin(i_4)} \frac{\partial H}{\partial \phi_4}, \quad (8)$$

$$\frac{d\phi_4}{dt} = -\frac{1}{L_4 \sin(i_4)} \frac{\partial H}{\partial i_4}. \quad (9)$$

Consequently, the semi-major axis and eccentricity remain constant during the orbital evolution. We then obtain

$$\frac{di_4}{dt} = \frac{15}{8} \frac{\beta}{(1-e_4^2)^2} e_b^2 \sin i_4 \sin 2\phi_4 \quad (10)$$

$$\frac{d\phi_4}{dt} = -\frac{3}{8} \frac{\beta}{(1-e_4^2)^2} \cos(i_4) (2 + 3e_b^2 - 5e_b^2 \cos(2\phi_4)) - \frac{d\varpi_b}{dt}, \quad (11)$$

where $d\varpi_b/dt$ is given by Equation (5) and

$$\beta = \frac{m_1 m_2}{m_b^2} \Omega_b \left(\frac{a_b}{a_4}\right)^{7/2} \quad (12)$$

is constant in time and is related to the magnitude of the nodal precession rate of the outer planet. Somewhat similar equations have been derived by Zanardi et al. (2018) in another context.

2.3 Resonance Condition

Equation (11) has a simple physical interpretation. It can be written as the sum of two contributions

$$\frac{d\phi_4}{dt} = \frac{d\Omega_{\text{inertial}}}{dt} + \frac{d\Omega_{\text{rot}}}{dt}. \quad (13)$$

The first term on the right hand side, $d\Omega_{\text{inertial}}/dt$, is the nodal precession rate of the outer planet due to the binary in the inertial frame, while the second term, $d\Omega_{\text{rot}}/dt$, is the nodal precession rate of the outer planet in the corotating frame due to the rotation of the reference frame. From the geometry of inclined orbits in the rotating frame, it follows that $d\Omega_{\text{rot}}/dt = -d\varpi_b/dt$.

For small inclination, $i_4 \approx 0$, a resonance is possible when $d\phi_4/dt = 0$ so that the outer planet's orbit evolves at constant nodal phase in the frame of the binary. From Equation (11), this is possible when the nodal precession rate of the particle in the inertial frame, the first term on the RHS of Equation (13) matches the apsidal precession rate of the binary $d\varpi_b/dt$. Since both are negative, resonance is possible. For a fixed set of the binary parameters a_b and e_b , we then expect that the resonance condition is satisfied for a range of the semi-major axis of the outer planet a_4 , since $\cos(2\phi_4)$ can take on values between -1 and +1. For values of ϕ_4 for which the RHS

of Equation (11) vanishes, the particle is locked at that phase since $d\phi_4/dt = 0$. The resonance condition then requires that

$$a_i < a_4 < a_o, \quad (14)$$

where

$$a_i = a_b \left(\left(\frac{a_3}{a_b}\right)^3 \frac{\sqrt{1-e_b^2}}{3(1-e_4^2)^2} \frac{m_1 m_2}{m_b m_3} \right)^{2/7} \quad (15)$$

and

$$a_o = a_b \left(\left(\frac{a_3}{a_b}\right)^3 \left(\frac{(1+4e_b^2)}{3(1-e_4^2)^2 \sqrt{1-e_b^2}} \right) \frac{m_1 m_2}{m_b m_3} \right)^{2/7}. \quad (16)$$

The dimensionless ratio of inner to outer radii is given by

$$\frac{a_i}{a_o} = \left(\frac{1-e_b^2}{1+4e_b^2} \right)^{2/7}. \quad (17)$$

This ratio increases with increasing binary eccentricity and is independent of the inner and outer planet eccentricities. For the case of a circular orbit outer planet, these critical radii reduce to equations (9) and (10) in Childs et al. (2023). The motion of the outer planet can undergo libration involving angle ϕ_4 , as we will see in the phase portrait in Figure 4. The orbit that satisfies the resonance condition is the largest librating orbit in a phase portrait and passes through the origin. Libration is also seen in Figure 2 of Childs et al. (2023).

2.4 Maximum Inclination

We use the fact that H given by Equation (4) is a constant of motion to determine the maximum inclination i_{max} of the initially coplanar outer planet. For an initially coplanar orbit, we have that

$$H_{i0} = -\frac{2\alpha}{(1-e_4^2)^{3/2}} (2 + 3e_b^2) - L_4 \frac{d\varpi_b}{dt}. \quad (18)$$

For librating orbits in the frame of the binary, the maximum inclination occurs for $di_4/dt = 0$ in Equation (10) and is for $\phi_4 = 90^\circ$, also as seen in Fig. 2 of Childs et al. (2023). In that case, H is given by

$$H_{i\text{max}} = \frac{\alpha}{(1-e_4^2)^{3/2}} \left[(2 + 3e_b^2)(1 - 3\cos^2(i_{\text{max}})) + 15e_b^2 \sin^2(i_{\text{max}}) \right] - L_4 \frac{d\varpi_b}{dt} \cos(i_{\text{max}}). \quad (19)$$

Setting $H_{i0} = H_{i\text{max}}$ we obtain

$$i_{\text{max}} = \arccos \left(-1 + 2x^{7/2} \right), \quad (20)$$

where

$$x = \frac{a_4}{a_o} \quad (21)$$

and a_o is given by Equation (16).

Equation (20) holds only for orbits at resonance, $a_i < a_4 < a_o$, because such orbits undergo libration. Thus, it holds for $[(1-e_b^2)/(1+4e_b^2)]^{2/7} < x < 1$. Notice that Equation (20) implies that i_{max} decreases with increasing a_4 and approaches zero as a_4 approaches a_o .

2.5 Inclination Instability

We show that the outer planet's inclination grows as a result of an instability. For i_4 exactly equal to zero, Equation (10) implies that i_4 remains at zero. But this state is unstable. We consider the case that the initial inclination $i_4(0) = i_0$ is nonzero and small. For $a_i < a_4 < a_o$, Equation (11) in lowest order is independent of i_4 and admits a solution for ϕ_4 which is constant in time. We denote that solution as ϕ_c and restrict the definition of ϕ_c to range from 0 to 90° . It is given by

$$\phi_c = \frac{1}{2} \arccos \left(\frac{2 + 3e_b^2 - 2x^{7/2}(1 + 4e_b^2)}{5e_b^2} \right). \quad (22)$$

It follows that $\phi_c = 0$ for $a_4 = a_i$ and $\phi_c = 90^\circ$ for $a_4 = a_o$. Using Equation (10), we find that the growth rate $\gamma_c = d \ln i / dt$ of the instability for small i_4 and $\phi_4 = \phi_c$ is constant in time. It is given by

$$\gamma_c = \frac{\lambda}{x^{7/2}} \sqrt{(1 - x^{7/2})(x^{7/2}(1 + 4e_b^2) - (1 - e_b^2))}, \quad (23)$$

where

$$\lambda = \frac{9}{4} \left(\frac{a_b}{a_3} \right)^3 \left(\frac{m_3}{m_b} \right) \sqrt{\frac{1 - e_b^2}{1 + 4e_b^2}} \Omega_b. \quad (24)$$

It follows that $\gamma_c = 0$ at $a_4 = a_i$ and $a_4 = a_o$ and is positive for $a_i < a_4 < a_o$. For $\phi_4 = \phi_c$, the inclination therefore grows exponentially. The growth rate is of order λ that is of order the binary apsidal precession rate $|d\varpi_b/dt|$ or faster provided that e_b is not small, as is shown below.

We consider a fixed set of system parameters but allow the outer planet semi-major axis to vary. The growth rate γ_c achieves a maximum value for an intermediate value of a_4 denoted by a_m that lies between a_i and a_o . It is given by

$$a_m = \left(\frac{1 - e_b^2}{1 + 3/2 e_b^2} \right)^{2/7} a_o. \quad (25)$$

The maximum growth rate is given by

$$\gamma_{\max} = \frac{45}{8} \left(\frac{a_b}{a_3} \right)^3 \frac{m_3}{m_b} \frac{e_b^2}{\sqrt{1 + 4e_b^2}} \Omega_b. \quad (26)$$

Notice that γ_{\max} is independent of the outer planet's eccentricity e and the binary mass ratio. We note, however, that the binary mass ratio cannot be too extreme. Otherwise, the approximation that the direct interaction of the inner planet with the outer planet is much less important than tidal interaction of the binary with the outer planet breaks down, as is explored in Section 4.5. For small binary eccentricity, this growth rate is quadratic in e_b , but varies almost linearly in e_b for larger binary eccentricity (see Figure 1). The change of inclination over a nodal precession period of the binary is given by

$$\Delta \ln i = \gamma_{\max} \frac{2\pi}{|d\varpi_b/dt|} = \frac{5\pi e_b^2}{\sqrt{(1 - e_b^2)(1 + 4e_b^2)}}. \quad (27)$$

Therefore a substantial growth of inclination can occur over an apsidal period of the binary provided that e_b is not small. It is large for high binary eccentricity.

2.6 General Initial Conditions

Equation (23) shows that inclination growth occurs exponentially fast for $a_i < a_4 < a_o$, until i_4 becomes of order unity, provided that

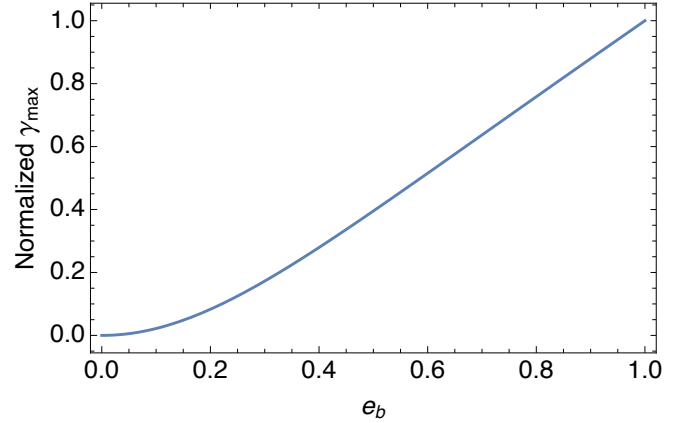


Figure 1. Normalized maximum growth rate of the inclination of an initially nearly coplanar outer planet as a function of binary eccentricity. The maximum is taken over the possible values of the planet semi-major axis with all other parameters fixed. The normalization factor is such that the plotted function is unity at $e_b = 1$ (see Equation (26)).

the initial nodal phase ϕ_0 equals ϕ_c . We explore the evolution of inclination for arbitrary initial phases ϕ_0 , again with small initial i_4 . For $0 < \phi_0 < 90^\circ$, Equation (11) has a solution

$$\phi_4(t) = \arctan \left(\tan(\phi_c) \frac{u_1(t)}{u_2(t)} \right), \quad (28)$$

where

$$u_1(t) = \tan(\phi_0) + \tan(\phi_c) \tanh(\gamma_c t), \quad (29)$$

$$u_2(t) = \tan(\phi_c) + \tan(\phi_0) \tanh(\gamma_c t). \quad (30)$$

On secular timescales, $\gamma_c t \gtrsim 1$, u_1 approaches u_2 and so $\phi_4(t)$ approaches ϕ_c by Equation (28). Other branches of the solution that occur outside this range of ϕ_0 can be constructed, but we do not show them.

For small i_4 and any ϕ_0 , Equations (10) and (11) have a solution for the instantaneous early growth rate $\gamma(t) = d \ln i / dt$ that is given by

$$\gamma(t) = \frac{u_1(t)u_2(t)\gamma_c}{u_1(t)^2 \sin^2 \phi_c + u_2(t)^2 \cos^2 \phi_c}. \quad (31)$$

For $0 < \phi_0 < 90^\circ$ and $180^\circ < \phi_0 < 270^\circ$, we have that $\sin(2\phi_0) > 0$ and so by Equation (10) the inclination initially grows, $\gamma(0) > 0$. In fact from Equation (31) it follows that $\gamma(t) > 0$ as long as i_4 remains small. In that case, from Equations (29) and (30), it follows that $u_1(t)$ approaches $u_2(t)$ on a timescale of γ_c^{-1} . This timescale is relatively short because many timescales γ_c^{-1} are required for the initially small inclination to grow to order unity values. Beyond that timescale, $\gamma(t)$ approaches γ_c and the growth becomes exponential in time.

We consider a fiducial model in which $m_1 = m_2 = 0.5m_b$, $e_b = 0.8$, $m_3 = 0.001m_b$, $a_3 = 5a_b$, $a = 15a_b$, $i_0 = 0.001$, and $e_3 = e_4 = 0$. In this case, Equations (15), (16), and (20), imply that $a_i = 12.1a_b$, $a_o = 23.4a_b$, and $i_{\max} = 4.37 = 125^\circ$. The upper panel of Figure 2 plots in blue $\gamma(t)/\gamma_c$ given by Equation (31) for a case with $\phi_0 = 45^\circ$. The growth rate initially varies, but settles to a constant value after a time of about $1/\gamma_c$. Also plotted are the results for $\gamma(t)$ (orange) and $i_4(t)$ (green) based on numerical integration of Equations (10) and (11) for the same parameters. As expected, there

is nearly exact agreement with the analytic results until i_4 in radians is of order unity.

However, for $90^\circ < \phi_0 < 180^\circ$ and for $270^\circ < \phi_0 < 360^\circ$, we have that $\sin(2\phi_0) < 0$ and from Equation (10) the inclination initially decays. Following an initial decay, the inclination grows. The time at which the γ reaches zero, denoted by t_1 , is determined by Equation (31) as

$$\gamma_c t_1 = \operatorname{arctanh} \left(\min \left(-\frac{\tan \phi_0}{\tan \phi_c}, -\frac{\tan \phi_c}{\tan \phi_0} \right) \right). \quad (32)$$

Since $\tan \phi_0 < 0$, we see that $t_1 > 0$. Notice that for $\phi_0 = -\phi_c$ or $\phi_0 = -\phi_c + 180^\circ$, time t_1 is infinite which is a consequence of the inclination $i_4(t)$ decaying exponentially at all times at rate γ_c . The initial time required for the inclination to grow, t_1 , decreases as ϕ_0 departs from $-\phi_c$.

The lower panel of Figure 2 plots in blue $\gamma(t)/\gamma_c$ given by Equation (31) for a case with $\phi_0 = -45^\circ$. The growth rate is initially negative, but settles to a constant value after a somewhat longer time than $1/\gamma_c$. As in the case of the upper panel, there is nearly exact agreement between with the analytic results until i_4 is of order unity. The results in the upper and lower panels are nearly identical, apart from a time shift, after the initial adjustment phase.

Figure 3 plots other cases that have $-90^\circ < \phi_4 < 0$ and initially negative growth rates. From this figure we see that for $\phi_0 = -\phi_c$, the inclination has a constant negative growth rate and $i_4(t)$ remains small at all times plotted, as expected by Equation (32). But for a slightly different value of ϕ_0 , the growth rate evolves to a positive value after a timescale considerably longer than $1/\gamma_c$. The initial peak of inclination is then delayed considerably. For a more negative initial nodal phase, the growth is less delayed, but occurs in a somewhat longer time than $1/\gamma_c$, as we also found in the lower panel of Figure 2. Overall, the delay time to exponential growth is of order $1/\gamma_c$ that is a single e-folding growth time during the exponential growth,

3 GEOMETRIC INTERPRETATION

The inclination instability of the outer planet can be understood in terms of a phase portrait as shown in Figure 4. The phase portrait plots $i_4 \sin(\phi_4)$ versus $i_4 \cos(\phi_4)$ for a few different orbits that pass close to $i_4 = 0$. For any point in the plot, the value of the outer planet inclination i_4 is its distance from the origin and the nodal phase ϕ_4 is its polar angle from the horizontal. The binary parameters are $m_1 = m_2 = 0.5m_b$ and $e_b = 0.8$. As the orbit approaches the origin $i_4 = 0$, as occurs in quadrants 2 and 4, its inclination decreases in time, in accordance with Equation (10). This decrease is indicated by red arrows in the figure. Similarly, as an orbit moves away from the origin as occurs in quadrants 2 and 4, its inclination increases in time, in accordance with Equation (10). This increase is indicated by the blue arrows in the figure. The phase trajectory that passes through the origin follows straight lines near the origin with a cusp at $i_4 = 0$. These lines lie on the separatrix between the librating orbits that undergo phase variations that are less than 360° to circulating orbits that undergo phase variations of 360° . In quadrant 1 this line is at angle $\phi_4 = \phi_c$ given by Equation (22). The inclination increases exponentially in time along this line at rate γ_c given by Equation (23). The orbit requires infinite time to depart from the origin along this line. If the orbit starts slightly away from the origin, the inclination grows in finite time to order unity values. Similarly, the orbit following the straight line in quadrant 4 undergoes exponentially decreasing inclination and requires infinite time to reach the origin. Orbits off the

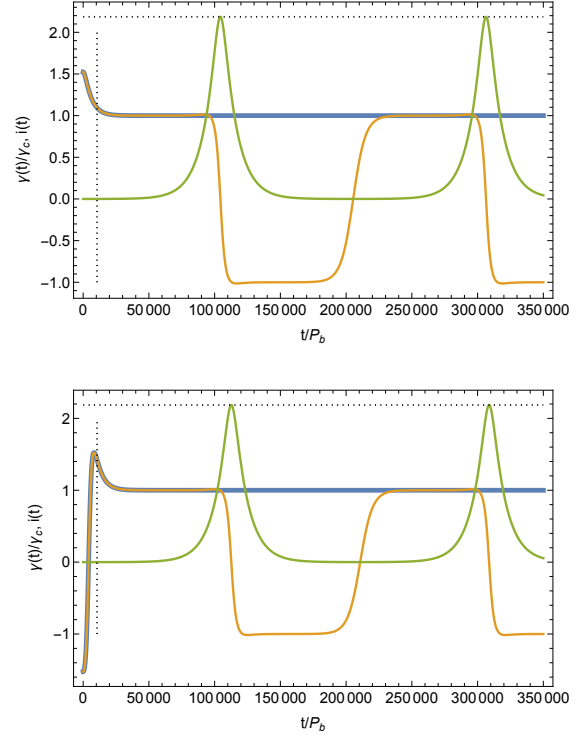


Figure 2. Inclination evolution of an outer planet orbiting at $a_4 = 15 a_b$ around an equal mass binary system of total mass $1M_\odot$ having binary eccentricity $e_b = 0.8$ and with an inner Jupiter-mass polar planet orbiting at $a_3 = 5 a_b$. Time is in units of binary orbital period P_b . The outer planet begins on a circular orbit and nearly coplanar to the binary orbit with inclination $i_0 = 0.0001$. The upper (lower) panel is for outer planet initial nodal phase $\phi_0 = 45^\circ$ ($\phi_0 = -45^\circ$). Plotted in blue is the normalized inclination growth rate determined by the analytic expression for $\gamma(t)/\gamma_c$ given by Equation (31) that is valid until i_4 becomes of order unity. Plotted in orange and green are respectively the normalized growth rates $1/\gamma_c d \ln i_4 / dt$ and inclination i_4 in radians obtained by integrating Equations (10) and (11). The dotted vertical line indicates a time of $1/\gamma_c$. The dotted horizontal line is the value of maximum inclination given by Equation (20). The analytically determined curve for the growth rate, derived in the small i_4 limit, follows the numerically determined curve until i_4 becomes of order unity.

straight lines never reach $i_4 = 0$ and always achieve order unity inclination (in radians) in finite time. The upper panel in Figure 2 shows initially growing inclination $\gamma > 0$, since it describes an orbit that starts in quadrant 1. The lower panels in Figure 2 and Figure 3 show initially decreasing inclination, since these orbits start in quadrant 4. But they later evolve to quadrant 3 where the inclination grows. An exception is the case of the green line in Figure 3 that lies along the straight line in quadrant 4 and has only decreasing inclination. It has phase $-\phi_c$ near the origin.

Notice that the orbits that start near the origin but not along the straight lines converge towards the straight line orbits at later time in quadrants 1 and 3 as the inclination grows. This is consistent with the behavior of the growth rates in Figures 2 and 3 that show evolution to the exponential growth rate γ_c for the straight line orbits.

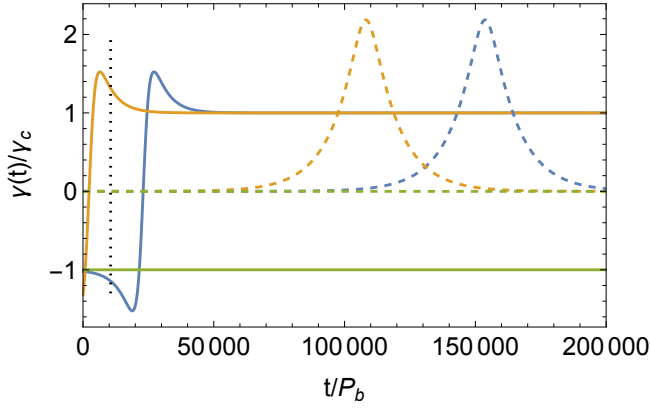


Figure 3. Normalized growth rates $\gamma(t)/\gamma_c$ (solid lines) given by Equation (31) and inclination i_4 in radians (dashed lines) as a function of time determined by numerical integration of Equations (10) and (11) for the parameters used in Figure 2, but with outer planet initial nodal phase $\phi_0 = -\phi_c = -0.358 = -20.51^\circ$ (green), $\phi_0 = -0.366 = -21^\circ$ (blue), and $\phi_0 = -\pi/3 = -60^\circ$ (orange). The dotted vertical line indicates a time of $1/\gamma_c$.

| Model | e_b | e_4 | q_b | a_i/a_b | a_o/a_b | $i_3(0)$ (deg) | i_0 (deg) |
|-------|-------|-------|-------|-----------|-----------|----------------|-------------|
| A1 | 0.2 | 0 | 1 | 14.0 | 14.8 | 88.7 | 0 |
| A2 | 0.2 | 0.5 | 1 | 16.5 | 17.4 | 88.7 | 0 |
| A3 | 0.2 | 0.5 | 0.5 | 15.9 | 16.8 | 88.7 | 0 |
| B1 | 0.5 | 0 | 1 | 13.5 | 17.8 | 89.3 | 0 |
| B2 | 0.5 | 0.5 | 1 | 15.9 | 21.0 | 89.3 | 0 |
| B3 | 0.5 | 0.5 | 0.5 | 15.4 | 20.3 | 89.3 | 0 |
| C1 | 0.8 | 0 | 1 | 12.1 | 23.4 | 89.7 | 0 |
| C2 | 0.8 | 0.5 | 1 | 14.3 | 27.6 | 89.7 | 0 |
| C3 | 0.8 | 0.5 | 0.5 | 13.8 | 26.6 | 89.7 | 0 |
| C4 | 0.8 | 0 | 1 | 12.1 | 23.4 | 89.7 | 2 |
| D1 | 0.8 | 0 | 0.5 | 11.7 | 22.6 | 89.7 | 0 |
| D2 | 0.8 | 0 | 0.1 | 8.8 | 17.0 | 89.2 | 0 |
| D3 | 0.8 | 0 | 0.01 | 4.8 | 9.3 | 83.4 | 0 |
| E1 | 0.8 | 0 | 0.1 | 8.8 | 17.0 | 89.2 | 1 |
| E2 | 0.8 | 0 | 0.01 | 4.8 | 9.3 | 83.4 | 1 |

Table 1. Simulation parameters. The first column is the simulation name. The second column is the binary eccentricity. The third column is the eccentricity of the outer planet. The fourth column is the binary mass ratio. The fifth column is the predicted inner semi-major axis of the unstable region given by Equation (15) and the sixth column is the predicted outer semi-major axis of the unstable region given by Equation (16). The seventh column i_3 is the initial inclination of the inner planet relative to the orbital plane of the binary in the generalised polar state. The eighth column i_0 is the initial inclination of the outer planet relative to the orbital plane of the binary.

4 COMPARISON WITH NUMERICAL SIMULATIONS

4.1 Models

We compare our analytic model with numerical simulations using the n -body code REBOUND (Rein & Liu 2012). We apply a set of models with parameters given by Table 1. The remaining parameters are described below. For all these models the inner planet has a mass of $0.001m_b$, an initial semi-major axis of $a_3 = 5a_b$, and is in generalized polar orientation (Martin & Lubow 2019). In a generalized polar orientation, the orbit of the outer planet is stationary in a frame that

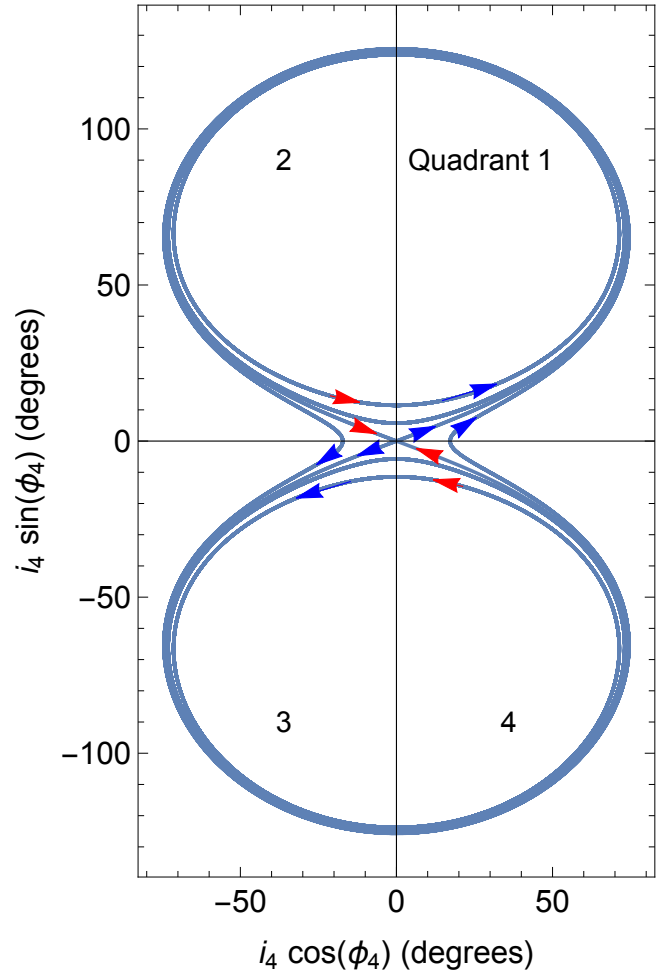


Figure 4. Phase portrait of $i_4 \cos(\phi_4)$ versus $i_4 \sin(\phi_4)$ for the system parameters described in Figure 2 based on the numerical integration of Equations (10) and (11). A few trajectories are plotted that pass near or through $i_4 = 0$. The blue (red) arrows indicate increasing (decreasing) inclination in time.

precesses with the binary. The longitude of the ascending node is equal to 90° , relative to the eccentricity vector of the binary. We determine the inclination for the generalized polar orientation to quadrupole order in the binary potential. A zero mass planet has a stationary orbit that is polar, with a tilt that is perpendicular to the binary orbital plane (e.g., Farago & Laskar 2010). But for a planet with nonzero mass, as we have here, this stationary orbit has a smaller tilt. Due to the nonzero inner plane mass, the binary has a small tilt relative to the invariable plane (the plane perpendicular to the total angular momentum of the system). In REBOUND, we apply a reference direction that is in the invariable plane and along the initial eccentricity vector of the binary projected onto that plane. For all models, the initial longitude of the ascending node for the binary and outer planet is -90° and for the inner planet is 90° . The initial argument of periapsis for all eccentric orbits is 90° . Unless otherwise stated, we present all inclinations as relative to the instantaneous orbital plane of the binary. We employ the IAS15 integrator (Rein & Liu 2012).

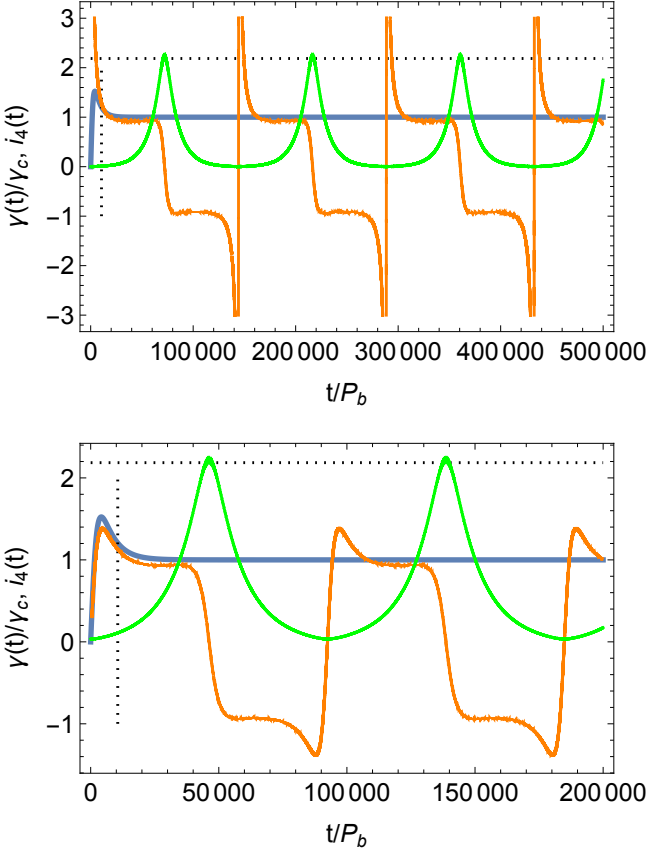


Figure 5. Plot of the inclination evolution of a massless outer planet with initial semi-major axis $a = 15a_b$ for Model C1 (upper panel) and C4 (lower panel). Plotted as green solid lines are inclination values i_4 in radians obtained from REBOUND simulations. Plotted as the orange solid lines are the normalized growth rates $1/\gamma_c d \ln i_4 / dt$ using i_4 from REBOUND simulations. The blue solid lines are the normalized inclination growth rates determined by the analytic expression for $\gamma(t)/\gamma_c$ given by Equation (31) that is valid until i_4 in radians becomes of order unity. The dotted vertical line indicates a time of $1/\gamma_c$. The dotted horizontal line is the predicted value of maximum inclination in radians given by Equation (20).

4.2 Inclination Oscillations

We consider the Models C1 and C4 in Table 1 with an initial semi-major axis of the outer planet of $15a_b$. This value of a lies between a_1 and a_0 and therefore i_4 is then expected to grow. The two models have the same parameters but differ in that for Model C1 the initial orbit of the outer planet is coplanar with the binary orbital plane (to numerical accuracy), while for Model C4 it is inclined by 2° . As expected, the numerical simulations show that the orbit of the outer planet undergoes inclination oscillations as plotted by green lines in Figure 5. The predicted maximum value (dotted horizontal line) agrees well with the peak values of the green lines in the simulations.

Plotted as blue lines in Figure 5 are the initial time dependent growth rates predicted by Equation (31) with initial longitude of ascending node of $\phi_0 = -90^\circ$. Recall that these rates are valid until i_4 in radians becomes of order unity. Plotted as orange lines are the inclination growth rates obtained from the simulations. However, for Model C1 (top panel) at early times $t < 1/\gamma_c$, there is disagreement between the analytic and numerical growth rates. The analytic model assumes that the binary lies in the invariable plane. But due to the

small mass outer planet there is a small tilt $\sim 0.8^\circ$ of the binary orbit away from this plane. We attribute this disagreement with that difference. For larger tilts of the outer planet the difference between the planes becomes less important to the inclination evolution. At later times the growth rates agree well over the inclination growing phase while $i_4 \lesssim 1$. For Model C4 that has a larger initial inclination there is good agreement in the growth rate evolution at all early times.

4.3 Effect of binary eccentricity

In Figure 6 we plot the maximum inclination achieved for the outer planet for Models An, Bn, and Cn for $n = 1, 2, 3$ listed in Table 1 as a function of the initial semi-major axis of the outer planet a_4 normalized by a_0 . For these cases the orbit of the outer planet is initially coplanar with the orbit of the binary. Three different initial values of binary eccentricity are considered. The values of a_4/a_0 on the horizontal axis can be easily transformed to a_4/a_b by applying the scaling factor a_0/a_b that is provided for each model in Table 1. For example, for the red dots in the bottom panel Figure 6 (Model C1), we have from Table 1 that the horizontal axis is multiplied by 23.4 to obtain a_4/a_b . The simulations are run for $10^6 P_b$, where P_b is the binary orbital period. As noted in Section 2, in the case that the outer planet is on a circular orbit or the binary has equal mass members, the octupole order terms vanish in the Hamiltonian and the analytic model should be more accurate. Models A1, B1, and C1 have $e_4 = 0$ and $q_b = 1$ and a vanishing octupole term. Models A2, B2, and C2 have $e_4 = 0.5$ and $q_b = 1$ and a vanishing octupole term. Models A3, B3, and C3 have $e_4 = 0.5$ and $q_b = 0.5$ and a nonvanishing octupole term. For given binary eccentricity, we ran simulations with a set of values for a_4/a_0 that is fixed for the three models, $n = 1, 2, 3$. The analytic model given by Equation (20) plotted by the solid blue lines predicts that the maximum value of the inclination is independent of n for a given model type (A, B, and C), for fixed $x = a_4/a_0$. Therefore, the three markers plotted by the red circle ($n = 1$), black circle ($n = 2$), and green circle ($n = 3$) should overlap.

Figure 6 shows overall good agreement between the analytic model and the simulations. The agreement is less good at low binary eccentricity $e_b = 0.2$ where the range of unstable radii is small. The agreement is best at high binary eccentricity $e_b = 0.8$, where the range of unstable radii is large. In that case, the circles overlap well and closely track the transition in a_4/a_0 from stable ($i_{\max} = 0$) to unstable inclination at $a_4 = a_1$. The case with intermediate binary eccentricity $e_b = 0.5$ shows good agreement but less so than the case with $e_b = 0.8$.

For all models at $a_4 \geq a_0$ the plotted values of maximum inclination are nonzero, while the analytic model predicts them to be zero. In the case of $e_b = 0.8$, we have from the simulations that $i_{\max} = 37^\circ$ at $a_4 = a_0$ which drops to $i_{\max} = 10^\circ$ at $a_4 = 1.07a_0$. We have investigated this effect and find that the orbits for $a_4 \gtrsim a_0$ are quite different from those described by the analytic model. Figure 7 shows the phase portrait of orbits at the outer semi-major axis of the unstable region a_0 . The plot shows that there is an asymmetry in that the orbits are not symmetric between the upper and lower half planes, such as as shown in Figure 4. The transition from resonant to nonresonant orbits near $a_4 = a_0$ involves a shift of the libration centers in both the upper and lower half planes to $i_4 = 0$. The plot shows a libration center occurs in the upper half-plane, but not in the lower half plane. This asymmetry is reversed if the initial nodal phase of the inner planet is changed by 180° . We attribute this effect to nonzero angular momentum of the inner planet that causes a small change in tilt of the binary orbit that is not taken into account in the analytic model.

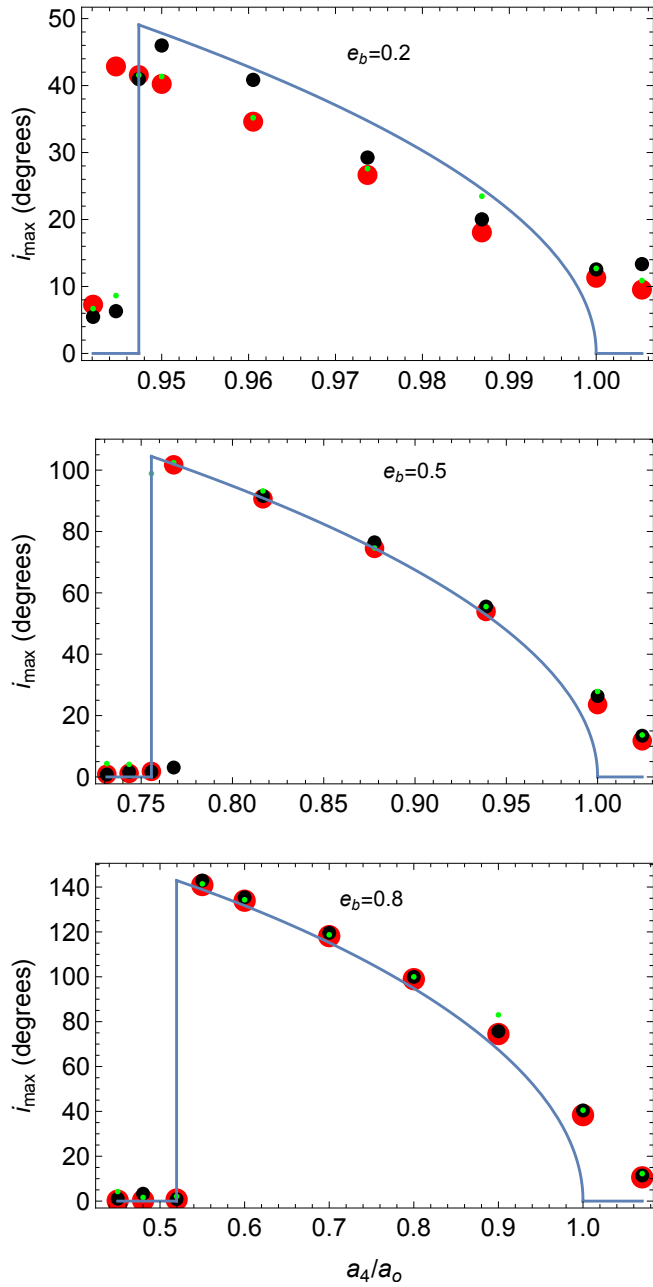


Figure 6. Maximum inclination of the outer planet relative to the binary orbital plane as a function of outer planet initial semi-major axis normalized by a_0 , the predicted outer semi-major axis of the unstable region, for three values of initial binary eccentricity. The `REBOUND` simulation results are plotted by large red circles for Models A1, B1, and C1, by black circles for Models A2, B2, and C2, and small green circles for Models A3, B3, and C3. The blue solid lines plot Equation (20) of the analytic model.

4.4 Effect of the initial semi-major axis of the outer planet

As noted in Section 2, we have assumed that the two planets are well enough separated so that the outer planet’s evolution is controlled by its interaction with the binary and that its interaction with the inner planet can be ignored. The agreement in Figure 6 between the analytic and numerical values for the maximum inclination indicates that this assumption holds for a_4 values in which the inclination instability occurs, $a_1 < a_4 < a_0$, in the models we considered. The

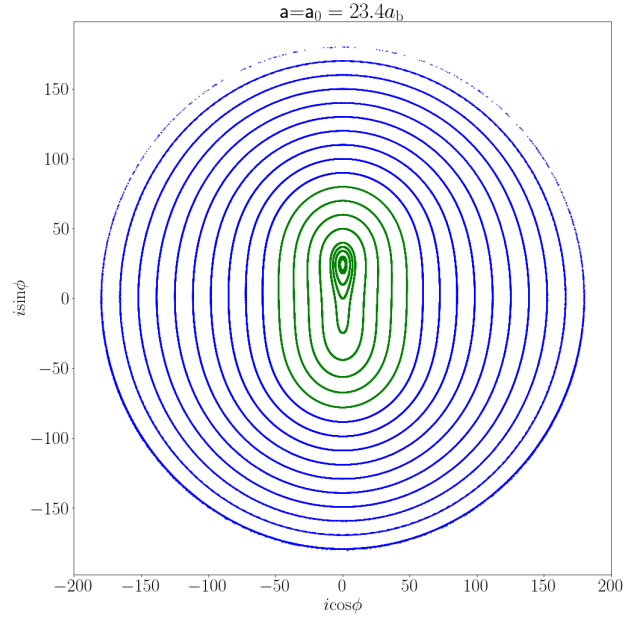


Figure 7. Phase portrait in degrees for the outer planet in a system with Model C1 parameters and outer planet orbital semi-major axis at $a_4 = a_0 = 23.4a_b$, where the analytic model predicts that the maximum inclination of an initially nearly coplanar orbit remains close to zero.

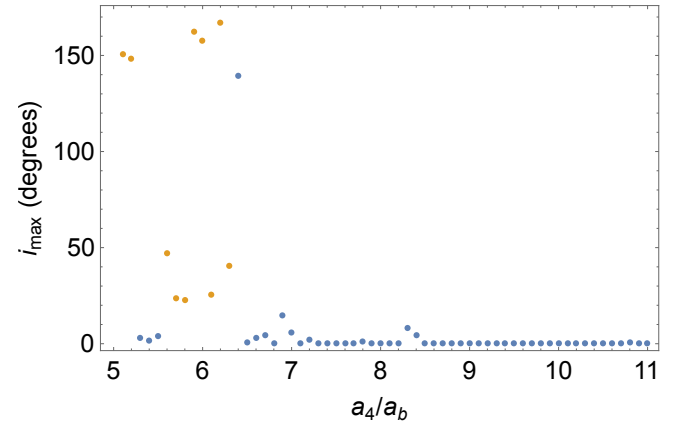


Figure 8. Plot of the outer planet maximum inclination relative to the binary orbital plane determined by `REBOUND` simulations for parameters in Model C1 as a function of initial semi-major axis normalized by a_b . The gold dots are for cases where the outer planet becomes unbound from the system, while the blue dots are for bound cases.

orbits of the two planets are generally in different planes. However, if $a_3 \approx a_4$, the two planets can interact strongly and the model in Section 2 can break down.

We explore this breakdown for Model C1 by extending the results plotted as red circles in the bottom panel of Figure 6 to smaller initial values of a_4 . Since such cases involve $a_4 < a_1$, the analytic model predicts that $i_{\max} = 0$. Figure 8 plots the values of i_{\max} as a function of the outer planet’s initial semi-major axis based on simulations. Gold dots denote cases where the outer planet becomes unbound from the system and blue dots denote cases where the outer planet remains bound over $10^6 P_b$. As seen from the plot, the breakdown

occurs for $a_4 \lesssim 7.0a_b$, where the outer planet is frequently ejected from the system. At larger values of a_4 , the inclination remains close to its initial value of zero. There are some deviations at $a_4 \approx 7a_b$ and $a_4 \approx 8.3a_b$. The latter case may involve the 2:1 resonance between the planets that occurs at $a_4 \approx 8.1a_b$. For the analytic model to hold, we require $a_{4\text{cr}} < a_i$, where $a_{4\text{cr}}$ is the critical semi-major axis of the outer planet for breakdown. From Equation (15), this requirement is then

$$\sqrt{\frac{a_b}{a_3}} \frac{\sqrt{1-e_b^2}}{(1-e_4^2)^2} \frac{m_1 m_2}{m_b m_3} > 3\chi^{7/2}, \quad (33)$$

where $\chi = a_{4\text{cr}}/a_3$. In the case of Figure 8, we have $\chi \approx 7/5 = 1.4$ and this inequality is well satisfied, as expected. More generally, this inequality should be satisfied if the object with mass m_3 is of planetary mass and is orbiting a binary star system with order unity mass ratio, provided that e_b is not very close to unity and that the inner planet is not very far from the binary. Some effects that occur outside this parameter range for extreme binary mass ratios are explored in the next subsection.

4.5 Effect of binary mass ratio

The approximations we have made in deriving the analytic model break down for sufficiently small binary mass ratio. The model assumes that the gravitational effects of the inner planet on the outer planet are much smaller than the gravitational effects of the binary. Childs et al. (2023) give a criterion for the analytic model breaking down when the nodal precession rate of the outer planet due to the inner planet is greater than the nodal precession rate due to the binary. This criterion can be used to provide a limit on the binary mass ratio

$$q_b > q_{\text{prec}}, \quad (34)$$

where for $q_{\text{prec}} \ll 1$ we have that

$$q_{\text{prec}} = \left(\frac{a_3}{a_b}\right)^2 \frac{m_3}{m_b} \frac{\tan i_4}{1 + 3/2 e_b^2}. \quad (35)$$

We apply a set of models with $e_b = 0.8$ and different binary mass ratios. The models we consider are Models C1, D1, D2, D3, E1, and E2 listed in Table 1. For all these models with $\tan i_4 \sim 1$, we have that $q_{\text{prec}} \sim 0.01$.

The analytic model ignores the interaction between the two planets. The outer semi-major axis for instability a_o decreases for small mass ratio but must be larger than the inner planet semi-major axis a_3 for the model to apply. For $a_4 \approx a_o \approx a_3$, strong interactions are expected to occur between the planets which are initially on mutually orthogonal orbits and the tilt instability described here would not apply. For $a_b \ll a_4 \ll a_o \approx a_3$, the planet could instead be subject to Kozai-Lidov oscillations (Kozai 1962; Lidov 1962) but modified by the inner binary (e.g., Martin et al. 2022). This requirement, $a_o > a_3$, implies a condition of the binary mass ratio

$$q_b > q_{\text{ppo}}, \quad (36)$$

where from Equation (16), for $q_{\text{ppo}} \ll 1$, we have that

$$q_{\text{ppo}} = \frac{3 \left(\frac{m_3}{m_b}\right) (1-e_4^2)^2 \sqrt{\frac{a_3}{a_b}} \sqrt{1-e_b^2}}{1+4e_b^2}. \quad (37)$$

For the models we consider, Models C1, D1, D2, D3, E1, and E2, we have that $q_{\text{ppo}} = 0.0011$.

We consider instead the weaker requirement that the semi-major axis of the outer planet for maximum growth rate be greater than the semi-major axis of the inner planet. This requirement, $a_m > a_3$, implies that

$$q_{\text{ppm}} = \frac{3 \left(\frac{m_3}{m_b}\right) (1-e_4^2)^2 \sqrt{\frac{a_3}{a_b}} (2+3e_b^2)}{2(1+4e_b^2)\sqrt{1-e_b^2}} \quad (38)$$

for $q_{\text{ppm}} \ll 1$.

We carried out simulations with $a_4 = a_m$ for Models C1, D1, D2, D3, E1, and E2. For all these models, we have that $q_{\text{ppm}} = 0.006$. and Equation (20) predicts that the maximum tilt is $i_{\text{max}} = 129.2^\circ$. Figure 9 plots the inclination evolution for a set of models (Models C1, D1, D2, and D3) that begin with an outer planet orbit that is coplanar with the binary orbital plane. For all these models, the maximum inclination agrees well with the predictions of the analytic model. For $q_b = 1$ and $q_b = 0.5$ the inclination oscillations have minima that are close to a tilt of zero.

For $q_b = 0.01$ and $q_b = 0.1$ the inclination minima are not close to zero. For $q_b = 0.01$, the binary mass ratio is of order of the minimum values based on the precession and planet-planet interaction criterion, $q_b \lesssim q_{\text{prec}} \sim q_{\text{ppm}}$. This is expected to lead to dramatically different changes in the orbital properties of the outer planet than the cases of higher values of q_b , as we show later.

Figure 10 compares the orbital evolution of two cases with $q_b = 0.1$ with the same initial parameters but with different initial inclinations. Plotted in orange is the initially coplanar case of Model D2, also plotted in orange in Figure 9, while plotted in black is Model E1 with a small initial inclination of 1° . The upper panel shows that the inclination minima are reduced considerably in Model E1. Secular theory in quadruple order predicts that the eccentricity of a circumbinary planet, ignoring planet-planet interactions, is constant that in this case should be zero. The eccentricity evolution of the outer planet shown in the lower panel is considerably different in the two cases. The eccentricities undergo complicated variations in time. In addition we find that the inner planet also acquires an oscillatory eccentricity with $0 \leq e_3 \lesssim 0.2$. The eccentricity $e_3(t)$ is identical in the two models because the outer planet has zero mass. We also find that the semi-major axis changes are very small $\sim 1\%$ in both cases. The sensitivity of the inclination minima to the initial inclination of the outer planet suggests that in this case the system is subject to the effects of a more complicated form of secular instability than given by our analytic model.

The case of Models D3 and E2 with $q_b = 0.01 \sim q_{\text{ppm}} = 0.006$ given by Equation (38) involves strong interactions between the two planets, resulting in a change in the motion of the outer planet. In these cases, the initial planet semi-major axis is $a_4 = 1.14a_3$. These two models again differ only in initial inclination of the outer planet. In Model D3, the outer planet orbit is initially coplanar with respect to the binary orbital plane, while in Model E2 the outer planet is inclined by 1° .

Figure 11 compares the orbital evolution of Models D3 and E2. Plotted in red is the case of Model D3, also plotted in red in Figure 9, while plotted in black is Model E2. The upper panel of Figure 11 shows that inclination oscillations occur in both cases but with different maxima and minima. Therefore, the good agreement between the analytic and simulation results in the inclination maxima for the red line in Figure 9 is not a general outcome and is sensitive to initial conditions. The middle panel plots the semi-major axis evolution of the outer planet in the two cases. The semi-major axis of the inner planet in these cases remains nearly constant, while its eccentricity undergoes mild oscillations with $0 \leq e_3 \lesssim 0.07$. In the initially copla-

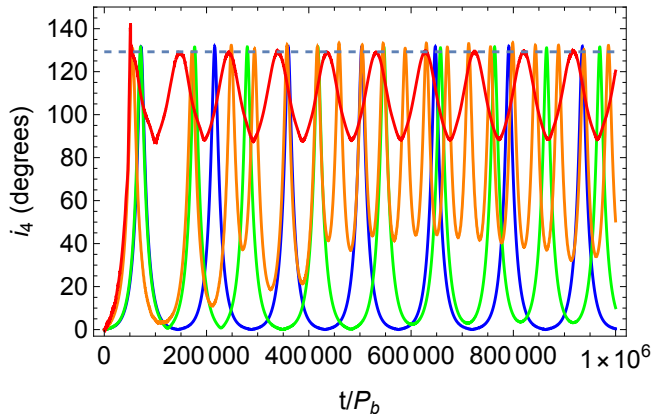


Figure 9. Solid lines plot the outer planet inclination evolution relative to the binary orbital plane determined by REBOUND simulations with different binary mass ratios. The outer planet orbit is initially coplanar with the binary orbital plane. The binary mass ratios are: $q_b = 1$ (blue, Model C1), 0.5 (green, Model D1), 0.1 (orange, Model D2), and 0.01 (red, Model D3). For each case, the value of the initial semi-major axis is $a_4 = a_m = 0.616a_o$ given by Equation (25). The horizontal dashed line is the predicted maximum inclination given by Equation (20) that has the same value for all these cases.

nar case (red), there is a close encounter at a time $\sim 5 \times 10^4 P_b$ that causes a jump in its semi-major axis that then remains fairly constant. In the initially inclined case (black), there is a jump in a_4 at an early time and a continual change in a_4 to large values.

As seen in the bottom panel of Figure 11, the periastron of the outer planet in red temporarily drops below the semi-major axis value for the inner planet. The orbits lie in different planes, so the orbits are not necessarily close. But in this case the orbital inclinations are nearly equal at the time of equal semi-major axis values. In the case of the outer planet shown in black, its periastron soon drops below the semi-major axis of the inner planet and remains in that state while its apastron is well beyond the semi-major axis of the inner planet. This leads to strong interactions with the inner planet and binary over long timescales which results in further energy and semi-major axis changes to the orbit of the outer planet.

4.6 Effect of the outer object mass

Up to this point we have considered the outer planet to be a test particle, $m_4 = 0$. In this section we analyze the effects of having $m_4 > 0$. We consider models with parameters given by Model B1 and C1 of Table 1 and outer object masses of $m_4/m_b = 0, 0.01, 0.01$ and also $m_4/m_b = 0.05, 0.1, 0.2$ and 0.3 for Model C1 which cover the range from planetary to stellar masses. We again determine i_{\max} , the maximum inclinations of the outer object orbit relative to the binary orbital plane using REBOUND simulations. The simulations are run for $10^6 P_b$. These cases are then similar to the red points in the middle and bottom panel of Figure 6 but with different outer object masses.

Figure 12 plots results for the different cases. Note that the horizontal axis is a_4 normalized by a_o , the predicted outer semi-major axis of the unstable region that assumes $m_4 = 0$. Since these models generally have $m_4 > 0$, the analytic curve in the panels may not be accurate, especially at larger values of m_4 . The upper two panels show that the predictions of the analytic model work well for $m_4 \leq 0.01 m_b$, which are typically in the planetary mass regime. For the case of $m_4 = 0.01 m_b$, we see that inner and outer semi-major

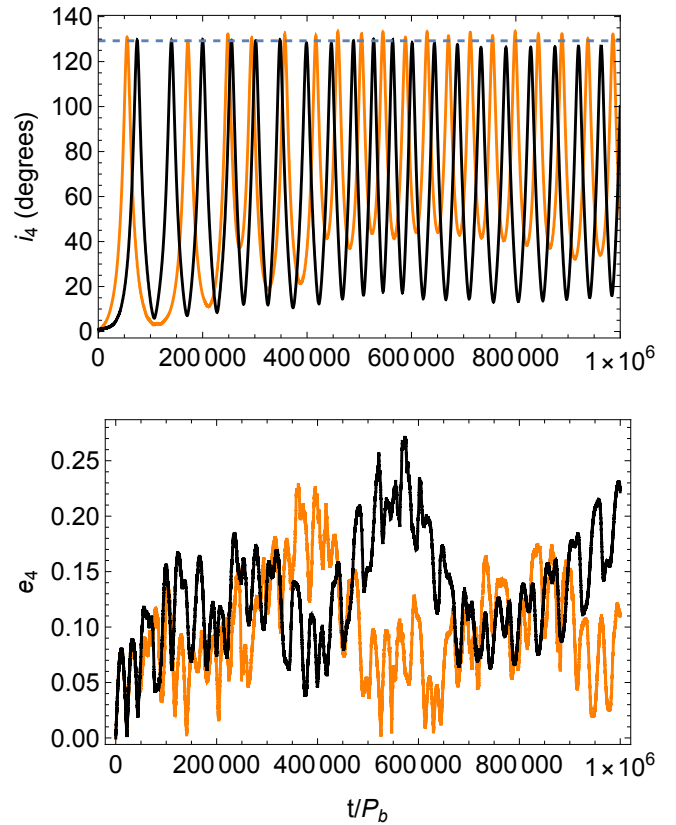


Figure 10. The upper panel plots the outer planet inclination evolution relative to the binary orbital plane determined by REBOUND simulations with binary mass ratio $q_b = 0.1$ for two initial inclinations. The lower panel plots the eccentricity evolution. The orange line is for an outer planet in Model D2 whose orbit is initially coplanar with the binary orbital plane. The solid black line is for an outer planet in Model E1 whose orbit is initially tilted by 1° with respect to the binary orbital plane. The horizontal dotted line in the upper panel is the predicted maximum inclination.

axes for the unstable region shifts outward. This shift is larger at lower binary eccentricity. The bottom panel Figure 12 shows that the instability is present even for stellar mass objects. The outward shift of the unstable zone increases with increasing values of m_4 . The unstable zone of $m_4 = 0.3 m_b$ lies completely outside the predicted unstable region for $m_4 = 0$ plotted as the blue solid line. The values of i_{\max} generally decrease with increasing values of m_4 but remain significant even at the highest value considered of $m_4 = 0.3 m_b$.

We further explored the nature of the instability at higher planet masses by examining the properties of the eccentricities and the inclinations relative to the invariable plane that is fixed in the inertial frame. The inclination variations relative to the invariable plane then are the inclination changes in the inertial frame. The results are plotted in Figure 13 for Model C1 with $m_4 = 0 m_b$ and $a_4 = a_m = 14.4 a_b$ in left panels and $m_4 = 0.3 m_b$ and $a_4 = 1.6 a_o = 37.4 a_b$ in the right panels. Generally, the results are very different for these two different outer object masses. The upper panels plot the inclinations relative to the invariable plane. The lower panels plot the inclinations relative to the orbital plane of the binary and also plot the binary eccentricity. The eccentricities of the inner planet and outer object that begin at zero remain small, less than 0.05 and 0.002, respectively, for both outer object masses.

For the case that $m_4 = 0$ the invariable plane nearly coincides

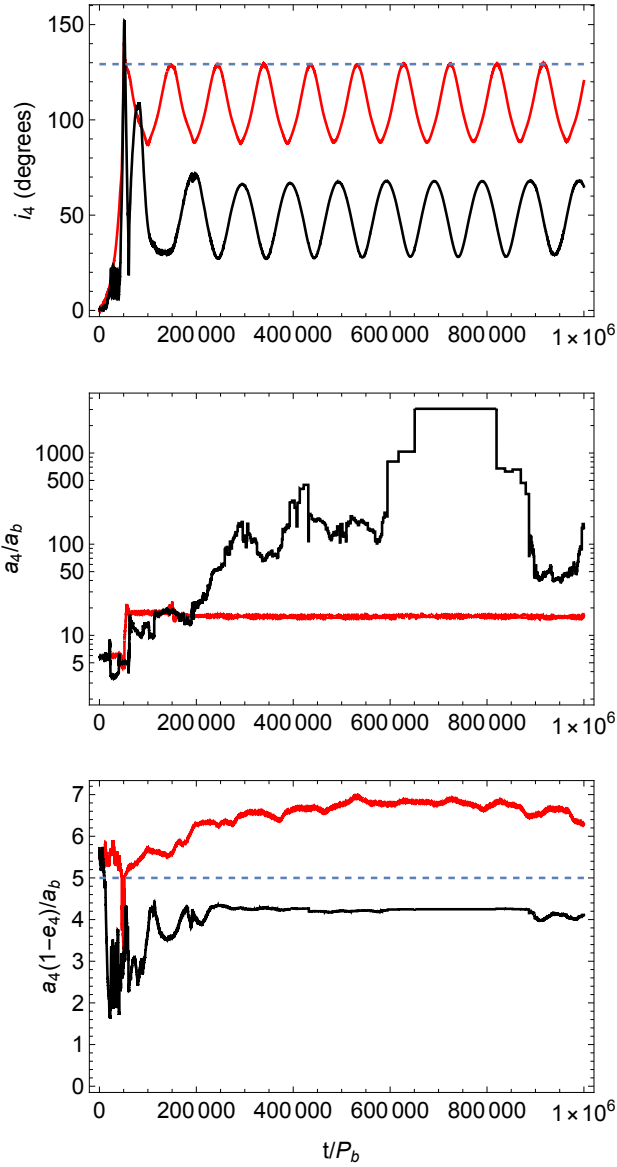


Figure 11. The top panel plots the outer planet inclination evolution relative to the binary orbital plane determined by `REBOUND` simulations with binary mass ratio $q_b = 0.01$ for two initial inclinations. The red line is for an outer planet in Model D3 whose orbit is initially coplanar with the binary orbital plane. The solid black line is for an outer planet in Model E2 whose orbit is initially tilted by 1° with respect to the binary orbital plane. The middle panel plots the semi-major axis evolution of the outer planet on a logarithmic scale. The bottom panel plots the periastron evolution of the outer planet. The horizontal dashed line in the top panel is the predicted maximum inclination. The horizontal dashed line in the bottom panel is the semi-major axis of the inner planet, a_3/a_b .

with the binary orbital plane because the binary contains nearly all of the system’s angular momentum. Consequently, the inclination of the binary orbit is nearly zero relative to the invariable plane as shown in the upper left panel of Figure 13. In addition, the inclination evolution for the inner planet are nearly the same in the upper and lower panels of Figure 13. The same also holds for the outer planet. The binary eccentricity remains nearly constant.

The case that $m_4 = 0.3m_b$ is much different. The angular momentum of the outer object dominates. Consequently, the inclination of

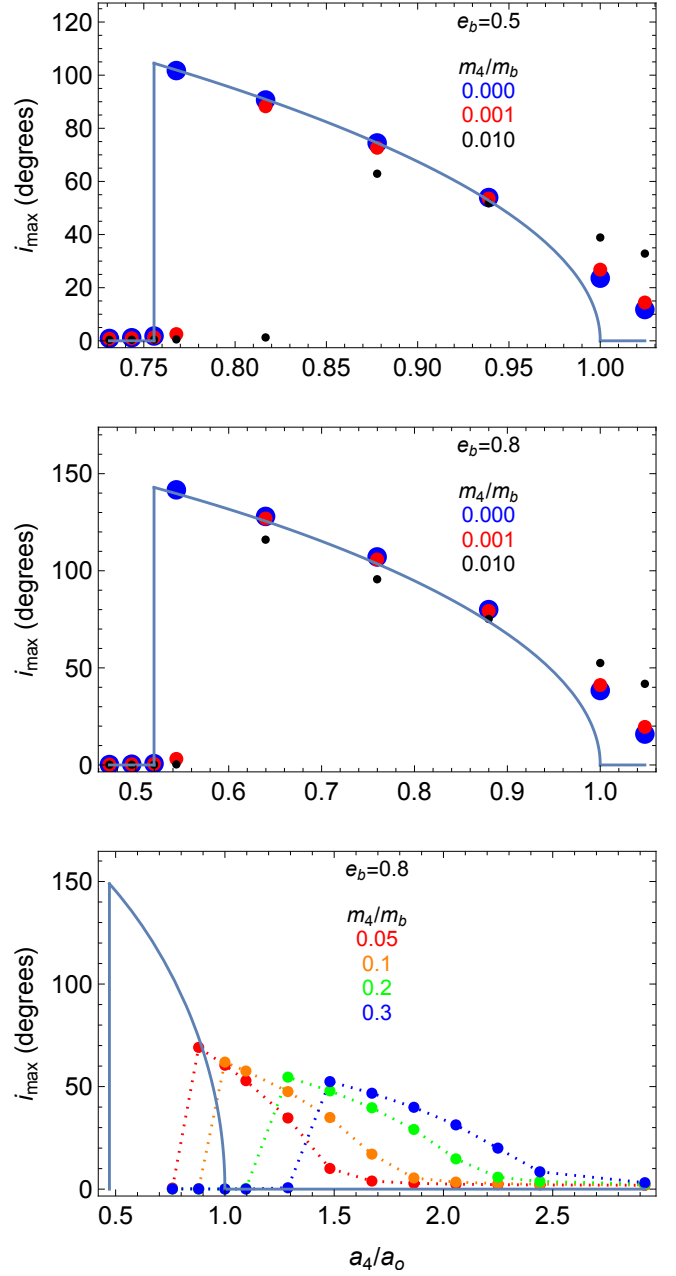


Figure 12. The top and middle panels plot as dots the outer planet maximum inclination relative to the binary orbital plane determined by `REBOUND` simulations for parameters in Models B1 and C1, respectively, as a function of initial semi-major axis normalized by a_0 , the predicted outer semi-major axis of the unstable region for a zero mass outer planet. The bottom panel is the same as the middle panel but for higher masses of the outer object. The dotted lines connect the dots. The blue solid lines plot Equation (20) of the analytic model. The circles in the bottom panel sometimes overlap for $i_{\max} = 0$.

the orbit of the outer object is smaller relative to the invariable plane than the inclination of the binary orbit that varies considerably, as seen in the upper left panel of Figure 13. In addition, the inclination of the orbit of the inner planet relative to the invariable plane varies considerably. However, in the lower panel of Figure 13 we see that the orbit of the inner planet remains nearly polar relative to the binary at all times. The eccentricity of the binary undergoes significant

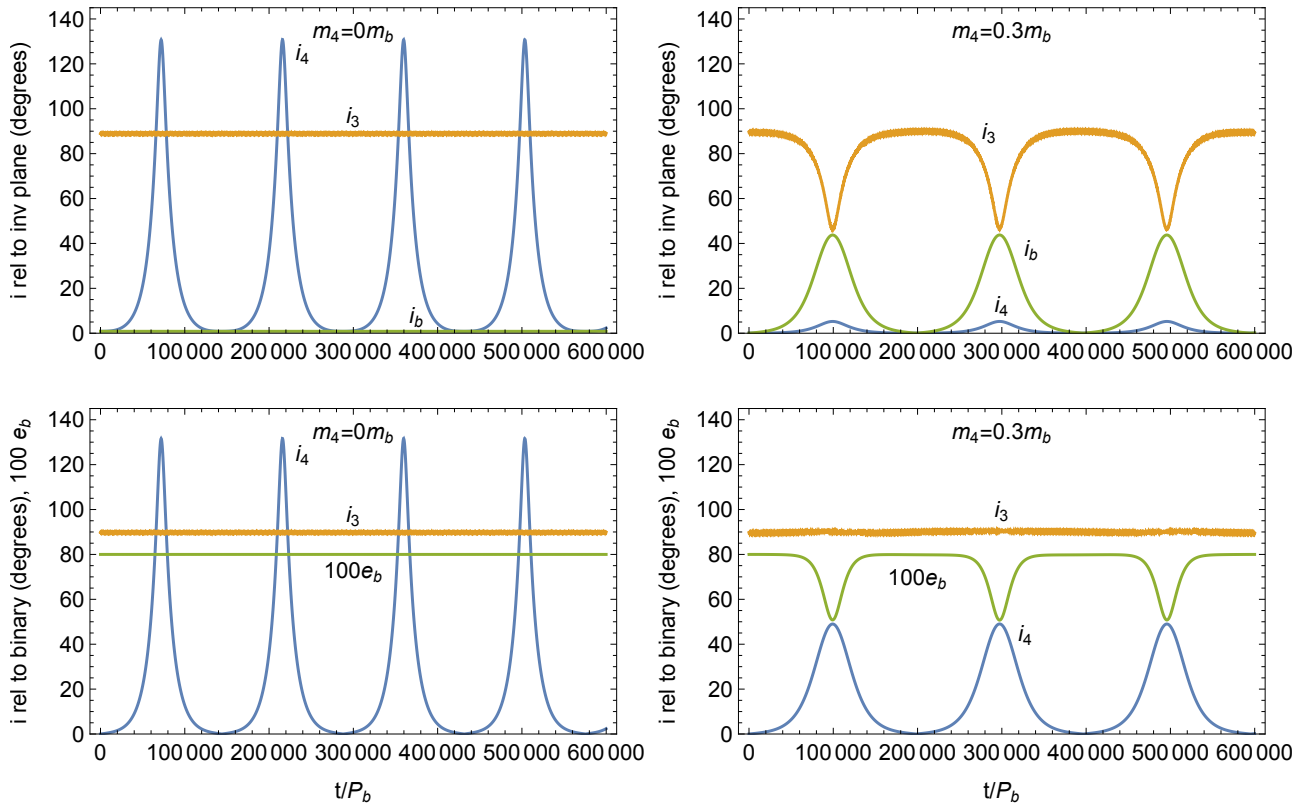


Figure 13. The panels plot the orbital element evolution determined by `REBOUND` simulations for parameters of Model C1 with $m_4 = 0$, $a_4 = 14.4a_b$ (left) and $m_4 = 0.3m_b$, $a_4 = 37.4a_b$ (right). The upper panels plot the inclination evolution relative to the invariable plane. The lower panels plot the inclination evolution relative to the binary orbital plane and also plots the binary eccentricity evolution.

variations. The inclination of the outer object relative to the binary is mainly due to inclination changes of the binary in the inertial frame.

5 DISCUSSION

The model presented describes an instability and resonance in the circumbinary case that in some ways is similar to what occurs around a binary member in Kozai-Lidov oscillations (KL) in the case of small initial particle eccentricity (Kozai 1962; Lidov 1962). In that case, there is a resonance in which the nodal precession frequency of the particle matches its apsidal precession frequency of the longitude of the periastron. In the case analyzed here, there is a resonance for small initial inclination in which the nodal precession frequency of the particle matches the apsidal precession frequency of the binary. In quadrupole order, there is an exponential growth of the initially small eccentricity in the KL case (e.g., Tremaine & Yavetz 2014; Lubow 2021) and exponential growth of an initially small inclination in the case described here.

Both cases involve particle orbit evolution along a separatrix (path that separates librating from circulating orbits and contains a cusp near the origin) in a phase portrait: $e \sin(\omega)$ versus $e \cos(\omega)$ in the KL case (e.g., Lubow 2021; Tremaine 2023) and $i \sin(\phi)$ versus $i \cos(\phi)$ in the current case as seen in Figure 4. Since the separatrix is a closed loop in both cases, they both involve secular oscillations. In both cases, the tilt of the straight line on the right side of the cusp in the separatrix corresponds to the phase that is then nearly constant in time, giving rise to resonance.

In both cases, the resonance occurs over a range of parameters.

In the KL case, there is a range of initial inclinations of the planet for which eccentricity instability occurs. In the current case, there is a range of initial orbital radii of the outer planet for inclination instability that increases with binary eccentricity as seen in Equation (17). The range of inclinations for eccentricity growth in the KL case occurs through the range of possible apsidal phases $0 \leq \omega < 360^\circ$ for which $d\omega/dt = 0$. This occurs at nearly fixed inclination while particle eccentricity remains small but grows. In the current case, the range of radii for inclination growth occurs through the range of possible nodal phases $0 \leq \phi < 360^\circ$ for which $d\phi/dt = 0$. In both cases, the stationary phase condition breaks down after a stage of exponential growth. In the KL case this breakdown occurs once order unity eccentricity values are achieved, for inclinations well above the critical angle. In the case analyzed here, this breakdown occurs once order unity inclination values (in radians) are achieved, for a_4 intermediate between a_i and a_o . Following the breakdown, there is a change in sign of the growth rate. Consequently, oscillations occur in both cases.

Apart from the similarity in growth in the two cases, there is some similarity in the analytic form for the evolution of the nodal phase. In the KL case the effects of the resonance cause a contribution to the evolution of the nodal phase of the form $\arctan(k_1 \tanh(k_2 t))$ for some constants in time k_1 and k_2 (see the last term on the RHS of equation (13) in Lubow (2021)). In the current case, the nodal phase evolution has the same form if $\phi_0 = 0$ in Equation (28).

Resonance is possible in the case analyzed here because the polar inner planet causes the binary to undergo retrograde precession that can match the retrograde nodal precession of the nearly coplanar outer planet. In the case of a nearly coplanar inner planet, the binary

would undergo prograde precession and the inclination instability would not occur, unless the outer planet is on a retrograde orbit.

Large inclination oscillations have also been previously analyzed in the context of retrograde particle orbits external to the Sun-Jupiter system (Zanardi et al. 2018). In this case, the binary consists of the Sun-Jupiter system and there is no inner planet to cause apsidal precession of the binary. Instead the Sun-Jupiter system undergoes prograde precession due to GR effects. A particle on an initially nearly coplanar retrograde orbit can undergo tilt oscillations due to the matching of the binary precession frequency with the nodal precession rate of the particle (e.g., Naoz et al. 2017; Lepp et al. 2022).

In the case that the outer object is of stellar mass, the inclination evolution of the planet in the inertial frame (i_3 in upper right panel of Figure 13) looks similar to what is expected to KL oscillations with high initial inclination (e.g., upper panel in Figure 1 of Lubow 2021). However, unlike KL oscillations, in this case e_3 undergoes small amplitude oscillations $0 \leq e_3 < 0.05$ and these oscillations are of much shorter period than the inclination oscillations.

With $m_4 = 0.3m_b$, as seen in the lower right panel of Figure 13, the inclination of the outer object relative to the binary orbit is maximum when the binary eccentricity is minimum, as occurs in KL oscillations. Unlike the KL case, the orbits of the binary and the outer object are initially coplanar and the binary must have a nonzero eccentricity. The vertical component of angular momentum of the binary (along the direction of the system angular momentum) is approximately constant in time, similar to the KL case.

6 SUMMARY

We have analyzed the orbital tilt stability of a system consisting of an eccentric orbit binary star and two circumbinary objects. The inner circumbinary object is a planet on a circular polar orbit about the binary, while the outer object is a planet or star that is initially on an orbit that is circular or eccentric and coplanar with respect to the binary. We find that due to the effects of the polar planet, a tilt instability occurs over a range of orbital semi-major axis values of the outer object, even if it is of stellar mass.

For the case that the outer object is a planet, we extended the recent results of Childs et al. (2023) to analytically determine the maximum inclination and initial time dependence of the inclination growth of the outer planet. We found that the inclination growth occurs as an instability that can be understood as the result of a resonance in which the nodal precession frequency of the outer planet matches the apsidal precession frequency of the binary. The resonance condition is satisfied over a broad range of outer planet radii, provided that the binary is sufficiently eccentric (see Equation (17)). Following a relatively short initial adjustment phase, the inclination growth occurs exponentially in time at a rate that is comparable to the absolute value of apsidal precession rate of the binary for moderate binary eccentricity. The growth rate increases with binary eccentricity (Figure 1). The inclination evolution can be understood in terms of trajectories in a phase portrait (see Figure 4). We tested the model with REBOUND simulations. The values of the maximum inclination achieved during the oscillations agree well with our analytic model, especially at high binary eccentricity, even if the outer planet is on an eccentric orbit (see Figure 6). As the binary mass ratio becomes extreme, the unstable zone of the outer planet shifts inwards. For sufficiently extreme binary mass ratios, the model breaks down and the evolution is dominated by other effects, such as strong planet-planet interactions (Figures 9 and 11).

If the outermost object is of stellar mass, the four bodies form a triple star system with a planet in a polar orbit about the central binary. Due to the effects of the polar planet on the apsidal precession rate of the binary, the binary orbit undergoes significant tilt oscillations for a range of orbital semi-major axis values of the outer star. The planet remains in a polar orbit about the binary as both it and the central binary undergo tilt oscillations (see right panels of Figure 13).

Nearly all the circumbinary planets that have been found were detected by the transit method using the Kepler and TESS telescopes (e.g., Welsh & Orosz 2018; Orosz et al. 2019; Kostov et al. 2020). This method relies on repeated transiting events of planets on orbits that are nearly coplanar with the binary orbital plane. The inclination instability would make the detection of planets in the instability zone very unlikely. Alternative methods of detection such as binary transit timing variations and binary Doppler measurements can detect non-coplanar circumbinary planets (Zhang & Fabrycky 2019; Standing et al. 2023).

It may be possible that initially coplanar gaseous circumbinary discs are subject to this instability, provided they are sufficiently long-lived. Part of the disc may lie within the unstable zone, while other parts that lie closer to the binary would be in the stable zone. For a disc that behaves rigidly, the overall effect of an inner stable region may weaken and even suppress the instability. But if it does not behave rigidly, the unstable portions might undergo tilt oscillations resulting in disc warping.

Circumbinary debris discs that are initially coplanar with the binary orbital plane could be subject to this instability. The solid bodies within the disc could undergo tilt oscillations whose properties are sensitive to their initial conditions. The instability could result in the vertical spreading of solid bodies that lie within the range of unstable semi-major axis values. Objects that are close together could lie on different orbital planes and undergo strong collisions. The end result might be an apparent gap in the disc.

ACKNOWLEDGEMENTS

AC acknowledge support from the NSF through grant NSF AST-2107738. RGM and SHL acknowledge support from NASA through grants 80NSSC19K0443 and 80NSSC21K0395. SHL thanks the Institute for Advanced Study for visitor support and thanks Scott Tremaine for a useful discussion.

DATA AVAILABILITY

The n -body simulation results can be reproduced with the REBOUND code (Astrophysics Source Code Library identifier ascl.net/1110.016) and the REBOUNDX code (Astrophysics Source Code Library identifier ascl.net/2011.020). The data underlying this article will be shared on reasonable request to the corresponding author.

REFERENCES

- Aly H., Dehnen W., Nixon C., King A., 2015, *MNRAS*, **449**, 65
- Bate M. R., 2018, *MNRAS*, **475**, 5618
- Chen C., Franchini A., Lubow S. H., Martin R. G., 2019, *MNRAS*, **490**, 5634
- Chen C., Lubow S. H., Martin R. G., 2020, *MNRAS*, **494**, 4645
- Chen C., Lubow S. H., Martin R. G., 2022, *MNRAS*, **510**, 351
- Chen C., Martin R. G., Lubow S. H., Nixon C. J., 2023a, *arXiv e-prints*, p. [arXiv:2310.15603](https://arxiv.org/abs/2310.15603)

Chen C., Lubow S. H., Martin R. G., Nixon C. J., 2023b, *MNRAS*, **521**, 5033
 Childs A. C., Martin R. G., Lepp S., Lubow S. H., Geller A. M., 2023, *ApJ*, **945**, L11
 Cuello N., Giuppone C. A., 2019, *A&A*, **628**, A119
 Czekala I., Chiang E., Andrews S. M., Jensen E. L. N., Torres G., Wilner D. J., Stassun K. G., Macintosh B., 2019, *ApJ*, **883**, 22
 Doolin S., Blundell K. M., 2011, *MNRAS*, **418**, 2656
 Facchini S., Lodato G., Price D. J., 2013, *MNRAS*, **433**, 2142
 Farago F., Laskar J., 2010, *MNRAS*, **401**, 1189
 Foucart F., Lai D., 2014, *MNRAS*, **445**, 1731
 Goldman I., Mazeh T., 1991, *ApJ*, **376**, 260
 Innanen K. A., Zheng J. Q., Mikkola S., Valtonen M. J., 1997, *AJ*, **113**, 1915
 Kennedy G. M., et al., 2012, *MNRAS*, **421**, 2264
 Kennedy G. M., et al., 2019, *Nature Astronomy*, **3**, 230
 Kenworthy M. A., et al., 2022, *A&A*, **666**, A61
 Kostov V. B., et al., 2020, *AJ*, **159**, 253
 Kozai Y., 1962, *AJ*, **67**, 591
 Lepp S., Martin R. G., Childs A. C., 2022, *ApJ*, **929**, L5
 Li G., Holman M. J., Tao M., 2016, *ApJ*, **831**, 96
 Lidov M. L., 1962, *Planet. Space Sci.*, **9**, 719
 Lubow S. H., 2021, *MNRAS*, **507**, 367
 Lubow S. H., Martin R. G., 2018, *MNRAS*, **473**, 3733
 Martin D. V., 2017, *MNRAS*, **465**, 3235
 Martin R. G., Lubow S. H., 2017, *The Astrophysical Journal*, **835**, L28
 Martin R. G., Lubow S. H., 2018, *MNRAS*, **479**, 1297
 Martin R. G., Lubow S. H., 2019, *MNRAS*, **490**, 1332
 Martin D. V., Triaud A. H. M. J., 2014, *A&A*, **570**, A91
 Martin D. V., Triaud A. H. M. J., 2015, *MNRAS*, **449**, 781
 Martin R. G., Lepp S., Lubow S. H., Kenworthy M. A., Kennedy G. M., Vallet D., 2022, *ApJ*, **927**, L26
 Naoz S., 2016, *ARA&A*, **54**, 441
 Naoz S., Li G., Zanardi M., de Elía G. C., Di Sisto R. P., 2017, *AJ*, **154**, 18
 Nixon C. J., King A. R., Pringle J. E., 2011, *MNRAS*, **417**, L66
 Nixon C., King A., Price D., 2013, *MNRAS*, **434**, 1946
 Orosz J. A., et al., 2019, *AJ*, **157**, 174
 Quarles B., Satyal S., Kostov V., Kaib N., Haghighipour N., 2018, *ApJ*, **856**, 150
 Raghavan D., et al., 2010, *ApJS*, **190**, 1
 Rein H., Liu S. F., 2012, *A&A*, **537**, A128
 Schneider J., 1994, *Planet. Space Sci.*, **42**, 539
 Smallwood J. L., Franchini A., Chen C., Becerril E., Lubow S. H., Yang C.-C., Martin R. G., 2020, *MNRAS*, **494**, 487
 Standing M. R., et al., 2023, *Nature Astronomy*, **7**, 702
 Tremaine S., 2023, *Dynamics of Planetary Systems*
 Tremaine S., Yavetz T. D., 2014, *American Journal of Physics*, **82**, 769
 Verrier P. E., Evans N. W., 2009, *MNRAS*, **394**, 1721
 Welsh W. F., Orosz J. A., 2018, in Deeg H. J., Belmonte J. A., eds., *Handbook of Exoplanets*. p. 34, doi:10.1007/978-3-319-55333-7_34
 Zanardi M., de Elía G. C., Di Sisto R. P., Naoz S., 2018, *A&A*, **615**, A21
 Zanardi M., de Elía G. C., Dugaro A., Coronel C. F., 2023, *MNRAS*, **525**, 2125
 Zanazzi J. J., Lai D., 2018, *MNRAS*, **473**, 603
 Zhang Z., Fabrycky D. C., 2019, *ApJ*, **879**, 92
 de Elía G. C., Zanardi M., Dugaro A., Naoz S., 2019, *A&A*, **627**, A17

where α is defined in Equation (2) and

$$h_1 = (2 + 3e_b^2) \left(1 - 3 \left(\frac{L_z}{L} \right)^2 \right), \quad (\text{A2})$$

$$h_2 = -15e_b^2 \cos(2\Omega_4) \left(1 - \left(\frac{L_z}{L} \right)^2 \right), \quad (\text{A3})$$

$$\Lambda = a_b^{3/2} \Omega_b \sqrt{a_4}, \quad (\text{A4})$$

$$L = a_b^{3/2} \Omega_b \sqrt{a_4(1 - e_4^2)}, \quad (\text{A5})$$

$$L_z = a_b^{3/2} \Omega_b \sqrt{a_4(1 - e_4^2)} \cos i_4. \quad (\text{A6})$$

The transformation to the rotating frame involves changing the canonical coordinates in Equations (A2) and (A3) to the rotating frame (in this case just Ω_4), while setting the canonical momenta to their values in the nonrotating frame. Consequently, the longitude of the ascending node Ω_4 in the nonrotating frame transforms to the longitude of the ascending node in the rotating frame that we denote by ϕ_4 . In addition, the orbital inclination $i_4 = \arccos(L_z/L)$, which is a function of the canonical momenta, does not change in transforming to the rotating frame, as expected. The Hamiltonian is also transformed to

$$H = H_{\text{npc}} - \Omega_f L_z, \quad (\text{A7})$$

where Ω_f is the rotation rate of the frame (Tremaine & Yavetz 2014; Tremaine 2023). Expressing the Hamiltonian of Equation (A7) in terms of variables ϕ_4 and i_4 , we obtain Equation (4) of the text.

We apply Hamilton's equations to Equation (A7) to obtain

$$\frac{d\Lambda}{dt} = -\frac{\partial H}{\partial \ell_4} = 0, \quad (\text{A8})$$

where ℓ_4 is the mean anomaly. This equation implies that a_4 is constant in time, as is stated in Equation (6) of the text. We also have that

$$\frac{dL}{dt} = -\frac{\partial H}{\partial \omega_4} = 0, \quad (\text{A9})$$

where ω_4 is the argument of periapsis. This equation and the constancy of a_4 imply that e_4 is constant in time, as is stated in Equation (7) of the text. Hamilton's equations also give that

$$\frac{dL_z}{dt} = -\frac{\partial H}{\partial \phi_4} \quad (\text{A10})$$

and

$$\frac{d\phi_4}{dt} = \frac{\partial H}{\partial L_z}, \quad (\text{A11})$$

which imply Equations (10) and (11) respectively in the text.

This paper has been typeset from a $\text{\TeX}/\text{\LaTeX}$ file prepared by the author.

APPENDIX A: TRANSFORMING TO THE ROTATING FRAME

The Hamiltonian in the nonrotating frame that is given by Equation (1) can be expressed in terms of Delaunay canonical variables (e.g., Tremaine 2023) as

$$H_{\text{npc}} = \alpha \left(\frac{\Lambda}{L} \right)^3 (h_1 + h_2), \quad (\text{A1})$$